

Quantum Computation of Electronic Transitions using a Variational Quantum Eigensolver

Robert M. Parrish,^{1,2,3,*} Edward G. Hohenstein,^{1,2} Peter L. McMahon,^{4,3} and Todd J. Martínez^{1,2}

¹ *Department of Chemistry and the PULSE Institute, Stanford University, Stanford, CA 94305*

² *SLAC National Accelerator Laboratory, Menlo Park, CA 94025*

³ *QC Ware Corporation, Palo Alto, CA 94301*

⁴ *E. L. Ginzton Laboratory, Stanford University, Stanford, CA 94305*

We develop an extension of the variational quantum eigensolver (VQE) algorithm – multistate, contracted VQE (MC-VQE) – that allows for the efficient computation of the transition energies between the ground state and several low-lying excited states of a molecule, as well as the oscillator strengths associated with these transitions. We numerically simulate MC-VQE by computing the absorption spectrum of an *ab initio* exciton model of an 18-chromophore light-harvesting complex from purple photosynthetic bacteria.

PACS numbers: 03.67.Ac,31.10.+z,31.15.-p

The accurate modeling of the many-body interactions in the ground and excited-state solutions of the electronic Schrödinger equation is a prerequisite for the quantitative prediction of molecular physical phenomena such as light harvesting. Using classical computers, this problem scales formally as the factorial of the number of involved electrons [1], via the solution of the full configuration interaction (FCI) equations, though many polynomial-scaling approximations such as density functional theory [2–5] (DFT), coupled cluster theory [6–9] (CC), density matrix renormalization group [10, 11] (DMRG), adaptive and/or stochastic configuration interaction methods [12–18] (CIPSI and variants), and semistochastic coupled cluster methods [19, 20], have been developed to combat this problem. Recently, there has been a surge of interest in using quantum computers to naturally solve the many-body electronic structure problem through methods such as the iterative phase estimation algorithm [21–26] (IPEA) or the variational quantum eigensolver [27–32] (VQE). However, the quartic-scaling complexity in number of molecular orbitals of the second-quantized electronic Hamiltonian, coupled with the overhead of encoding the fermionic antisymmetry of the electrons through the Jordan-Wigner [33, 34] (JW), Bravyi-Kitaev [35, 36] (KB), or superfast Bravyi-Kitaev [37, 38] (SFKB) transformations, implies that rather long circuit depths will be required to directly model the electronic structure problem. We also point out a recent approach [39–41] that might formally reduce this complexity to quadratic or linear via a tensor hypercontraction representation [42–44] of the potential. In the present work, we explore a domain- and problem-specific means to reduce the complexity of the representation of the electronic structure problem in quantum computing: an *ab initio* exciton model [45–49]. For large-scale photoactive complexes consisting of a number of nonbonded chromophore units, the *ab initio* exciton model compresses the details of the electronic structure on each chromophore into a handful of monomer electronic states. The determination of

the full configuration interaction wavefunctions describing the mixing of monomer electronic states in the full complex remains a formidable task - here we show that this might be a natural computational task for a near-term quantum computer.

Another area that deserves exploration is the development of efficient quantum algorithms for the even-handed treatment of ground- and excited-state energies and transition properties, e.g., for the computation of absorption spectra. There exist IPEA-type algorithms for excited states, such as the WAVES protocol [50] or the variational swap test [51], but we focus on VQE-type methods here. Most existing VQE-type quantum algorithms are “state specific,” meaning that they optimize the VQE parameters for one state at a time. Examples include the folded spectrum (FS) method [27], which requires the observation of the square of the Hamiltonian, or the orthogonality-constrained VQE (OC-VQE) method [52, 53] which applies a penalty term to remove contaminants from lower-lying states. Another, more-global approach is the quantum subspace expansion (QSE-VQE) [54, 55], which first performs VQE to determine the ground state, and then determines the excited states by classical diagonalization in a basis of response states. QSE-VQE treats all the excited states on a similar footing, but by construction favors the ground state, and requires the determination of three- and four-particle density matrices through high-order Pauli measurements.

MC-VQE - Inspired by the mixed quantum/classical strategy of QSE-VQE (particularly the final classical diagonalization step), we have developed a new multistate, contracted variant of VQE (MC-VQE), which aims to (1) treat the ground and a handful of excited states on the same footing (2) minimize the size of the classical subspace that must be diagonalized and (3) provide for the straightforward computation of transition properties such as oscillator strengths. MC-VQE takes the following

ansatz for a number (N_Θ) of eigenstates of interest,

$$|\Psi_\Theta\rangle \equiv \hat{U} \sum_{\Theta'} |\Phi_{\Theta'}\rangle V_{\Theta'\Theta}. \quad (1)$$

Here $|\Phi_\Theta\rangle$ are a set of contracted, orthonormal “reference” states, which are obtained by solving a classical electronic structure problem such as configuration interaction singles (CIS). By contracted, we mean that these reference states are generally taken to be a linear combination of Hilbert-space configurations - ideally this will allow the reference states to be reasonably accurate approximations to the exact eigenstates. As will be seen, all that we will require is that we have an efficient quantum circuit to prepare the “diagonal” state $|\Phi_\Theta\rangle$ and the “interfering” state $(|\Phi_\Theta\rangle \pm |\Phi_{\Theta'}\rangle)/\sqrt{2}$. For CIS reference states, this is possible - see the Supplemental Material for a detailed circuit [56] which generalizes a previously known circuit for $|W_N\rangle$ states [57].

The operator $\hat{U}(\{\eta\})$ is the VQE entangler matrix, an orthogonal Hilbert-space matrix constructed from a set of two-qubit entangling operators whose set of parameters $\{\eta\}$ will be chosen to maximally decouple $\{|\Phi_{\Theta'}\rangle\}$ from the rest of the Hilbert space, i.e., to approximately block diagonalize the Hamiltonian. The matrix $V_{\Theta'\Theta}$ is an $N_\Theta \times N_\Theta$ orthogonal matrix that describes the rotation of the entangled contracted states $\{|\chi_{\Theta'}\rangle \equiv \hat{U}|\Phi_{\Theta'}\rangle\}$ to the approximate eigenbasis $\{|\Psi_\Theta\rangle\}$. This matrix can be determined by classical diagonalization of the entangled contracted Hamiltonian,

$$H_{\Theta''\Theta'} V_{\Theta'\Theta} = V_{\Theta''\Theta} E_\Theta : V_{\Theta'\Theta} V_{\Theta'\Theta''} = \delta_{\Theta\Theta''}. \quad (2)$$

The eigenvalues E_Θ are the Ritz approximations to the exact eigenvalues. The entangled contracted Hamiltonian is,

$$H_{\Theta\Theta'} \equiv \langle \Phi_\Theta | \hat{U}^\dagger \hat{H} \hat{U} | \Phi_{\Theta'} \rangle. \quad (3)$$

The diagonal matrix elements can be evaluated by partial tomography measurements in a quantum computer, as is done in standard VQE:

$$H_{\Theta\Theta} = \langle \Phi_\Theta | \hat{U}^\dagger \hat{H} \hat{U} | \Phi_\Theta \rangle. \quad (4)$$

The (real) off-diagonal matrix elements can also be obtained from observable quantities:

$$\begin{aligned} 2H_{\Theta\neq\Theta'} &= (\langle \Phi_\Theta | + \langle \Phi_{\Theta'} |) \hat{U}^\dagger \hat{H} \hat{U} (| \Phi_\Theta \rangle + | \Phi_{\Theta'} \rangle) / 2 \\ &- (\langle \Phi_\Theta | - \langle \Phi_{\Theta'} |) \hat{U}^\dagger \hat{H} \hat{U} (| \Phi_\Theta \rangle - | \Phi_{\Theta'} \rangle) / 2. \end{aligned} \quad (5)$$

This highlights the need for quantum circuits to prepare the “interfering” state $(|\Phi_\Theta\rangle \pm |\Phi_{\Theta'}\rangle)/\sqrt{2}$.

The parameters of the MC-VQE entanglement circuit should be chosen to maximally decouple the full set of approximate eigenstates $\{|\Psi_\Theta\rangle\}$ from the rest of the Hilbert

space. This can be accomplished in a 2-norm sense in the Hamiltonian by optimizing the parameters of the VQE entangler operator to minimize the state-averaged energy,

$$\bar{E} = \frac{1}{N_\Theta} \sum_{\Theta} E_\Theta = \frac{1}{N_\Theta} \sum_{\Theta} H_{\Theta\Theta}. \quad (6)$$

The second equality follows from the definition of the trace, and shows that the minimization of the state-averaged energy is equivalent to the minimization of the sum of diagonal contracted Hamiltonian matrix elements.

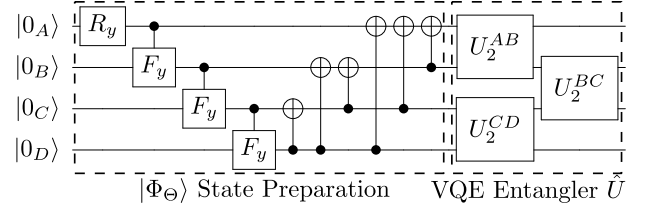


FIG. 1: Example MC-VQE quantum circuit for $N = 4$ linear exciton model. The first stage prepares contracted CIS reference states $|\Phi_\Theta\rangle$ [or interference variations $(|\Phi_\Theta\rangle \pm |\Phi_{\Theta'}\rangle)/\sqrt{2}$ thereof] specified by rotation angles in the R_y and F_y gates. The second stage applies the many-body VQE entangler \hat{U} specified through a polynomial number of rotation angles 2-body U_2 entangler gates. 1- and 2-body Pauli measurements of this circuit then determine the entangled contracted Hamiltonian matrix elements $H_{\Theta\Theta'}$.

Overall the MC-VQE algorithm has four stages:

1. Classically solve CIS or some other polynomial-scaling electronic structure problem to “sketch out” the shapes of the relevant states by determining the contracted reference states $\{|\Phi_\Theta\rangle\}$.
2. Vary the parameters of the VQE entangler operator to optimize the state-averaged energy $\bar{E} = (1/N_\Theta) \sum_{\Theta} H_{\Theta\Theta}$.
3. For the converged VQE entangler operator, observe the reference-state Hamiltonian $H_{\Theta\Theta'}$ using sums and differences of Hamiltonian expectations of interference states.
4. Classically diagonalize $H_{\Theta\Theta'}$ to obtain the Ritz estimates of the eigenstates and eigenvalues.

A schematic of the quantum circuit needed to prepare a CIS state $|\Phi_\Theta\rangle$ and apply the VQE entangler \hat{U} is shown in Figure 1 - details of this circuit are available in the Supplemental Material [56]. Overall, the MC-VQE approach has a number of unique features relative to established excited-state VQE approaches such as quantum subspace expansion (QSE-VQE) [54]:

- The VQE entangler \hat{U} is optimized in a state-averaged manner, providing a balanced treatment of ground and excited states, i.e., all states are computed to approximately equal accuracy.
- The optimization of the VQE entangler \hat{U} requires only the measurement of N_Θ diagonal matrix elements $H_{\Theta\Theta}$. The determination of the N_Θ^2 off-diagonal matrix elements $H_{\Theta\neq\Theta'}$ can be done separately, after the VQE entangler parameters have been optimized.
- Higher-order density matrices are not required.

Note that the eigenstates can be reexpressed as $|\Psi_\Theta\rangle \equiv \hat{U}|\Gamma_\Theta\rangle$ where $\{|\Gamma_\Theta\rangle \equiv \sum_{\Theta'} |\Phi_{\Theta'}\rangle V_{\Theta'\Theta}\}$ are rotated reference states. The algorithm above is quite general - we present a demonstration below for the case of the *ab initio* exciton model, but it is clear that this approach might be immediately applicable to the efficient computation of excited states in fermionic electronic structure computations. Transition properties (such as the transition dipole moment, needed for computing the absorption spectrum) can also be computed by substituting the desired operator \hat{O} in place of \hat{H} in Equation 5.

It is worth noting that MC-VQE can be roughly pictured either as a generator of the wavefunction ansatz of Equation 1 or as a means to observe the elements of the unitarily-transformed effective Hamiltonian of Equation 4, wherein the VQE entangler operator \hat{U} acts as a wave operator [58, 59].

Ab Initio Exciton Model - Consider a set of N chromophoric monomers, each labeled by index A , which are arranged in a particular nuclear geometry in a photoactive complex. In isolation, the chromophores are usually characterized by a constant number of photoactive electronic states, regardless of the number of electrons in the monomer (often between two and four states are photoactive in the visible spectrum in the monomer: the ground and the first few singlet excited states). If the monomers are sufficiently far apart in the full photoactive complex (e.g., if they are at noncovalent separations due to embedding in a protein scaffold), the strict considerations of fermionic antisymmetry can be relaxed without loss of accuracy, and the full complex electronic eigenstates can be computed as a configuration interaction of direct products of monomer states. I.e., for electronic state Θ in a system where each chromophoric monomer is characterized by the ground state $|0_A\rangle$ and the first excited state $|1_A\rangle$ (a restriction we make from here onward to facilitate ease of mapping to qubits), the electronic states are,

$$|\Psi_\Theta\rangle = \sum_{p_0, q_1 \dots \in [0,1]} C_{p_0 q_1 \dots r_{N-1}}^\Theta |p_0\rangle \otimes |q_1\rangle \otimes \dots \otimes |r_{N-1}\rangle. \quad (7)$$

Typically, we wish to find these adiabatic electronic states, e.g., to determine the energy gaps and oscillator strengths in the system as a proxy for the electronic absorption spectrum. Formally, this requires diagonalization of the exciton Hamiltonian, which can straightforwardly be written in Pauli matrix notation for the special case considered here of a photoactive system with two electronic states per monomer,

$$\begin{aligned} \hat{H} = \mathcal{E} + \mathcal{H}^{(1)} + \mathcal{H}^{(2)} = \mathcal{E}\hat{I} + \sum_A \mathcal{Z}_A \hat{Z}_A + \mathcal{X}_A \hat{X}_A \quad (8) \\ + \sum_{A>B} \mathcal{X}\mathcal{X}_{AB} \hat{X}_A \otimes \hat{X}_B + \mathcal{X}\mathcal{Z}_{AB} \hat{X}_A \otimes \hat{Z}_B \\ + \mathcal{Z}\mathcal{X}_{AB} \hat{Z}_A \otimes \hat{X}_B + \mathcal{Z}\mathcal{Z}_{AB} \hat{Z}_A \otimes \hat{Z}_B. \end{aligned}$$

The choice of Hamiltonian matrix elements $\{\mathcal{Z}_A, \mathcal{X}_A, \mathcal{Z}\mathcal{Z}_{AB}, \mathcal{Z}\mathcal{X}_{AB}, \mathcal{X}\mathcal{Z}_{AB}, \mathcal{X}\mathcal{X}_{AB}\}$ for a given photoactive complex is an interesting art. Choosing these parameters empirically to match experiment or other reference data is the crux of the phenomenological Frenkel-Davydov exciton model [60, 61]. Recently, we introduced a new *ab initio* exciton model approach [45–49], in which the parameters of the exciton model are determined explicitly by high-level *ab initio* computations on the isolated monomers, under the assumption of sufficient monomer separations to relax the fermionic antisymmetry constraint. We have extended the *ab initio* exciton model to treat full non-adiabatic dynamics through the development of analytical gradients/coupling vectors [46, 47] and have increased the basis set to include both local and charge-transfer excitations [47].

In this *ab initio* exciton model the Hamiltonian matrix elements in Equation 8 all have distinct physical origins: \mathcal{E} is the mean-field energy, \mathcal{Z}_A is roughly (half) of the difference between the ground and excited state energy of monomer A , $\mathcal{X}\mathcal{X}_{AB}$ is the transition-dipole–transition-dipole interaction and $\mathcal{Z}\mathcal{Z}_{AB}$ is the difference-dipole–difference-dipole interaction between monomers A and B , and $\mathcal{X}\mathcal{Z}_{AB}$ and $\mathcal{Z}\mathcal{X}_{AB}$ are transition-dipole–difference-dipole interaction cross terms. \mathcal{Z}_A and \mathcal{X}_A carry Fock-matrix like dressings from the mean-field electrostatic environment of the system. A full definition of the matrix elements is available in the Supplemental Material [56].

Diagonalizing this Hamiltonian to obtain the eigenstates $\{|\Psi_\Theta\rangle\}$, even for a model of this simplicity, is difficult classically due to the 2^N dimension of the Hilbert space $|p_0\rangle \otimes |q_1\rangle \otimes \dots \otimes |r_{N-1}\rangle$. To highlight this, we point out that this part of the problem is usually solved classically in a highly restricted Hilbert space where only single excitations are allowed [45–47]: for many energy-transfer applications this may be reasonable, but will be incapable of describing the conical intersection between the ground

and lowest-excited states [62]. However, it is apparent that the *ab initio* exciton Hamiltonian is entirely isomorphic to an extended spin-lattice Hamiltonian. Therefore, existing technologies for the quantum simulation of spin-lattice Hamiltonians should provide utility for this problem. Below, we demonstrate the potential for this mapping by simulating the quantum computation of the absorption spectrum of a large photoactive complex using MC-VQE. Note that we are not the first to propose a crossover between exciton models for photoactive complexes and spin-lattice models in qubits: there have been myriad prior studies using phenomenological exciton models to theoretically characterize [63–65] or physically simulate [66–69] the exciton energy transfer (EET) process in open systems such as the Fenna-Matthews-Olsen (FMO) complex. However, the emphasis in the prior literature has been on the modeling of the dissipative non-adiabatic dynamics of EET through coupling with the protein/solvent environment in an effective way (via effective phonon coupling approaches such as the Holstein model). In our approach, we emphasize the accurate *ab initio* computation of the electronic absorption spectrum at a given nuclear configuration, as a prerequisite for direct non-adiabatic dynamics simulations.

Demonstration - MC-VQE circuits were implemented in our in-house quantum simulator package, QUASAR. All aspects of state preparation, VQE entanglement, and casting of transition matrix elements as difference observables were performed in the simulator, though 1- and 2-body Pauli expectation values were evaluated through contractions of wavefunction amplitudes (equivalent to infinite averaging of discrete Pauli measurements), and noise/error channels were not modeled. CIS is solved classically in the basis of the reference and all singly-excited configurations. We avoid the “barren plateaus” issue of locating optimized VQE parameters [70] by finding a tightly converged and near-global-optimal solution for the 108 MC-VQE parameters which is directly downhill from a zero-entanglement guess in 14 L-BFGS iterations, using finite-difference gradients [56].

For a practical test case, an *ab initio* exciton model was constructed for the $N = 18$ cyclical LH2 B850 ring complex of the purple photosynthetic bacteria - the specific geometry is provided in the Supplemental Material [56]. Monomer Hamiltonian matrix elements were computed in the GPU-accelerated TERACHEM program [71–73] for classical electronic structure theory, using TDA-TD-DFT [4] at $\omega\text{PBE}(\omega = 0.3)/6\text{-}31\text{G}^*$ [74, 75]. Dimer Hamiltonian matrix elements were approximated by the dipole/transition-dipole model. Dimer Hamiltonian matrix elements were truncated after cyclical nearest-neighbor contacts due to the r_{AB}^{-3} decay of the interactions. Figure 2 depicts the simulated absorption spectrum of this *ab initio* exciton model computed from the excitation energies and oscillator strengths of the lowest 18 electronic transitions with MC-VQE and

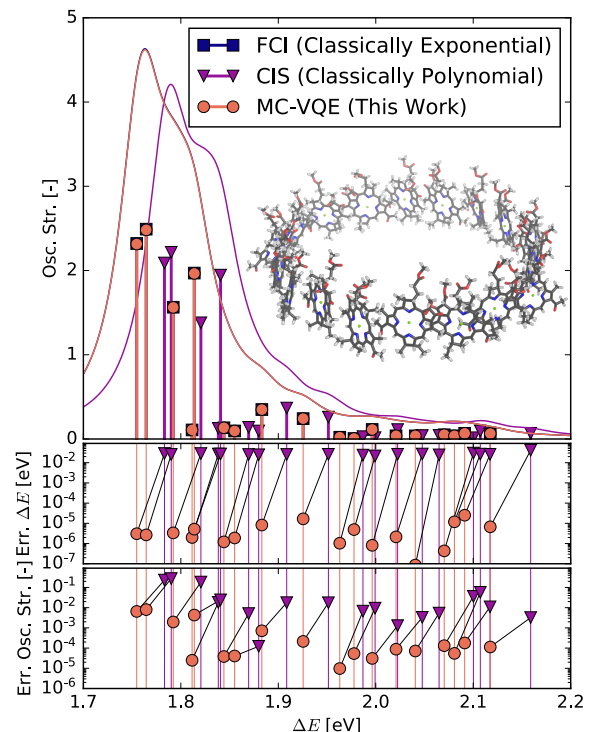


FIG. 2: (color online). Top - Simulated absorption spectrum of $N = 18$ cyclical LH2 B850 ring complex (geometry depicted in inset), computed from the excitation energies and oscillator strengths of the lowest 18 electronic transitions, depicted as vertical sticks. The envelope of the absorption spectrum is sketched by broadening the contribution from each transition with a Lorentzian with width of $\delta = 0.05$ eV. The simulated MC-VQE and reference FCI results are visually indistinguishable. Middle - errors in excitation energies. Bottom - errors in oscillator strengths. Middle and bottom - thin lines are a guide for the eye.

CIS, and compared to the “full configuration interaction” (FCI) reference computed in the space of all possible 2^N monomer excitation configurations. The CIS absorption shows a noticeable blue shift of a few hundredths of an eV relative to FCI, and, more noticeably, the CIS oscillator strengths may deviate by 10% or more, particularly for the brightest states. By contrast, MC-VQE with a single entangler layer is visually indistinguishable from FCI - the maximum deviations of excitation energies are on the order of tens of μeV , while the oscillator strengths generally deviate by $\ll 1\%$. At the request of a reviewer, we have also considered a test case where CIS produces qualitatively incorrect results relative to FCI: an $N = 8$ linear stack of BChl-a chromophores. MC-VQE has no trouble with this system, and again produces results which are essentially visually indistinguishable from FCI: see the Supplemental Material for full details [56].

Outlook - In this Letter, we have demonstrated a hybrid quantum/classical approach for the modeling of

electronic absorption spectra in large-scale photoactive complexes by using a multistate, contracted variant of VQE (MC-VQE) in the context of an *ab initio* exciton model. We simulated MC-VQE for an $N = 18$ LH2 B850 complex (a Hilbert space dimension of $2^{18} = 262144$). The MC-VQE absorption spectrum matches FCI quantitatively with only a single layer of VQE two-body entanglers with a connectivity matching that of the exciton Hamiltonian. With a qubit count equivalent to the number of monomers N , a circuit depth that is linear in N , a gate count that is quadratic in N , and a requirement of only 1- and a sparse set of 2-body Pauli measurements, MC-VQE applied to an *ab initio* exciton model with local Hamiltonian connectivity is a compelling application for deployment to near-term quantum hardware.

This Letter is intended to sketch the salient features of the MC-VQE algorithm and its potential application to the *ab initio* exciton model. Future work will investigate robustness of the algorithm on realistic hardware including the influence of gate/measurement errors. *Ab initio* exciton Hamiltonians with more-complicated local connectivity that are unlikely to be addressable with classical methods such as DMRG should also be investigated. Beyond this, effort should be devoted to direct implementation on real hardware, where circuit locality and simplification/sparsification will be of key importance. Finally, MC-VQE should be explored in the context of direct simulation of fermionic electronic structure problems - it seems highly likely that this algorithm will be easily adaptable to the study of multiple excited states in many types of Hamiltonians beyond the *ab initio* exciton model.

Note added during revision: After the first revision of our paper was released, we learned of the “subspace search” VQE (SS-VQE) approach developed by Nakanishi, Mitarai, and Fujii in a recent preprint [76]. Both SS-VQE and MC-VQE use a state-averaged VQE entangler \hat{U} , and both describe how to compute transition properties. The methods have several key differences: SS-VQE uses hybrid quantum-classical optimization to determine the minimal and maximal eigenvectors in the subspace matrix, while MC-VQE uses classical diagonalization of the subspace Hamiltonian to determine all subspace eigenstates simultaneously. Additionally, MC-VQE uses contracted reference states (e.g., from CIS) while SS-VQE uses Hilbert-space configurations.

Acknowledgements: This material is based on work partially supported by the U.S. Department of Energy, Office of Science, Office of Advanced Scientific Computing Research, Scientific Discovery through Advanced Computing (SciDAC) program.

Financial Disclosure: TJM is a cofounder of PETACHEM LLC. RMP and PLM own stock/options in QC WARE CORP.

-
- * Electronic address: rob.parrish@qcware.com
- [1] T. Helgaker, P. Jørgensen, and J. Olsen, *Molecular Electronic Structure Theory*, Wiley, New York, 2000.
 - [2] P. Hohenberg and W. Kohn, Phys. Rev. **136**, B864 (1964).
 - [3] W. Kohn and L. J. Sham, Phys. Rev. **140**, A1133 (1965).
 - [4] E. Runge and E. K. Gross, Phys. Rev. Lett. **52**, 997 (1984).
 - [5] W. Koch and M. C. Holthausen, *A Chemist’s Guide to Density Functional Theory*, Wiley-VCH, New York, 2001.
 - [6] J. Čížek, J. Chem. Phys. **45**, 4256 (1966).
 - [7] G. D. Purvis and R. J. Bartlett, J. Chem. Phys. **76**, 1910 (1982).
 - [8] T. D. Crawford and H. F. Schaefer, *An Introduction to Coupled Cluster Theory for Computational Chemists*, pages 33–136, Wiley-Blackwell, 2007.
 - [9] I. Shavitt and R. Bartlett, *Many-Body Methods in Chemistry and Physics: MBPT and Coupled-Cluster Theory*, Cambridge Molecular Science, Cambridge University Press, 2009.
 - [10] S. R. White, Phys. Rev. Lett. **69**, 2863 (1992).
 - [11] G. K.-L. Chan and S. Sharma, Ann. Rev. Phys. Chem. **62**, 465 (2011).
 - [12] C. F. Bender and E. R. Davidson, Phys. Rev. **183**, 23 (1969).
 - [13] B. Huron, J. Malrieu, and P. Rancurel, J. Chem. Phys. **58**, 5745 (1973).
 - [14] G. H. Booth, A. J. Thom, and A. Alavi, J. Chem. Phys. **131**, 054106 (2009).
 - [15] D. Cleland, G. Booth, and A. Alavi, J. Chem. Phys. **132**, 041103 (2010).
 - [16] A. A. Holmes, N. M. Tubman, and C. Umrigar, J. Chem. Theory Comput. **12**, 3674 (2016).
 - [17] J. B. Schriber and F. A. Evangelista, J. Chem. Phys. **144**, 161106 (2016).
 - [18] J. B. Schriber and F. A. Evangelista, J. Chem. Theory Comput. **13**, 5354 (2017).
 - [19] J. E. Deustua, J. Shen, and P. Piecuch, Phys. Rev. Lett. **119**, 223003 (2017).
 - [20] J. E. Deustua, I. Magoulas, J. Shen, and P. Piecuch, J. Chem. Phys. **149**, 151101 (2018).
 - [21] D. S. Abrams and S. Lloyd, Phys. Rev. Lett. **79**, 2586 (1997).
 - [22] D. S. Abrams and S. Lloyd, Phys. Rev. Lett. **83**, 5162 (1999).
 - [23] A. Aspuru-Guzik, A. D. Dutoi, P. J. Love, and M. Head-Gordon, Science **309**, 1704 (2005).
 - [24] B. P. Lanyon et al., Nat. Chem. **2**, 106 (2010).
 - [25] D. Wecker, B. Bauer, B. K. Clark, M. B. Hastings, and M. Troyer, Phys. Rev. A **90**, 022305 (2014).
 - [26] N. M. Tubman et al., arXiv preprint arXiv:1809.05523 (2018).
 - [27] A. Peruzzo et al., Nat. Comm. **5**, 4213 (2014).
 - [28] J. R. McClean, J. Romero, R. Babbush, and A. Aspuru-Guzik, New J. Phys. **18**, 023023 (2016).
 - [29] P. OMalley et al., Phys. Rev. X **6**, 031007 (2016).
 - [30] A. Kandala et al., Nature **549**, 242 (2017).
 - [31] J. R. McClean et al., arXiv preprint arXiv:1710.07629 (2017).
 - [32] J. Romero et al., Quant. Sci. Tech. **4**, 014008 (2018).

- [33] P. Jordan and E. Wigner, *Z. Phys.* **47**, 631 (1928).
- [34] G. Ortiz, J. E. Gubernatis, E. Knill, and R. Laflamme, *Phys. Rev. A* **64**, 022319 (2001).
- [35] S. B. Bravyi and A. Y. Kitaev, *Ann. Phys.* **298**, 210 (2002).
- [36] J. T. Seeley, M. J. Richard, and P. J. Love, *J. Chem. Phys.* **137**, 224109 (2012).
- [37] K. Setia and J. D. Whitfield, *arXiv preprint arXiv:1712.00446* (2017).
- [38] K. Setia, S. Bravyi, A. Mezzacapo, and J. D. Whitfield, *arXiv preprint arXiv:1810.05274* (2018).
- [39] R. Babbush et al., *arXiv preprint arXiv:1706.00023* (2017).
- [40] I. D. Kivlichan et al., *Phys. Rev. Lett.* **120**, 110501 (2018).
- [41] M. Motta et al., *arXiv preprint arXiv:1808.02625* (2018).
- [42] E. G. Hohenstein, R. M. Parrish, and T. J. Martínez, *J. Chem. Phys.* **137**, 044103 (2012).
- [43] R. M. Parrish, E. G. Hohenstein, T. J. Martínez, and C. D. Sherrill, *J. Chem. Phys.* **137**, 224106 (2012).
- [44] R. M. Parrish, E. G. Hohenstein, N. F. Schunck, C. D. Sherrill, and T. J. Martínez, *Phys. Rev. Lett.* **111**, 132505 (2013).
- [45] A. Sisto, D. R. Glowacki, and T. J. Martinez, *Acc. Chem. Res.* **47**, 2857 (2014).
- [46] A. Sisto et al., *Phys. Chem. Chem. Phys.* **19**, 14924 (2017).
- [47] X. Li, R. M. Parrish, F. Liu, S. I. Kokkila Schumacher, and T. J. Martínez, *J. Chem. Theory Comput.* **13**, 3493 (2017).
- [48] A. F. Morrison, Z.-Q. You, and J. M. Herbert, *J. Chem. Theory Comput.* **10**, 5366 (2014).
- [49] A. F. Morrison and J. M. Herbert, *J. Phys. Chem. Lett.* **6**, 4390 (2015).
- [50] R. Santagati et al., *Sci. Adv.* **4**, eaap9646 (2018).
- [51] S. Endo, T. Jones, S. McArdle, X. Yuan, and S. Benjamin, *arXiv preprint arXiv:1806.05707* (2018).
- [52] O. Higgott, D. Wang, and S. Brierley, *arXiv preprint arXiv:1805.08138* (2018).
- [53] J. Lee, W. J. Huggins, M. Head-Gordon, and K. B. Whaley, *J. Chem. Theory Comput.* (2018).
- [54] J. R. McClean, M. E. Kimchi-Schwartz, J. Carter, and W. A. de Jong, *Phys. Rev. A* **95**, 042308 (2017).
- [55] J. I. Colless et al., *Phys. Rev. X* **8**, 011021 (2018).
- [56] See Supplemental Material at doi:XX.XXXX/XX for detailed derivation/definition of the Hamiltonian matrix elements, for technical details of the CIS state preparation, MC-VQE entangler circuits, and output of the MC-VQE optimization profile, and for an additional case study with increased multi-excitonic character.
- [57] F. Diker, *arXiv preprint arXiv:1606.09290* (2016).
- [58] P. Durand, *Phys. Rev. A* **28**, 3184 (1983).
- [59] D. Maynau, P. Durand, J. Daudey, and J. Malrieu, *Phys. Rev. A* **28**, 3193 (1983).
- [60] J. Frenkel, *Phys. Rev.* **37**, 17 (1931).
- [61] A. S. Davydov, *Physics-Uspekhi* **7**, 145 (1964).
- [62] B. G. Levine, C. Ko, J. Quenneville, and T. J. Martínez, *Mol. Phys.* **104**, 1039 (2006).
- [63] M. B. Plenio and S. F. Huelga, *New J. Phys.* **10**, 113019 (2008).
- [64] F. Caruso, A. W. Chin, A. Datta, S. F. Huelga, and M. B. Plenio, *J. Chem. Phys.* **131**, 09B612 (2009).
- [65] F. Caruso, A. W. Chin, A. Datta, S. F. Huelga, and M. B. Plenio, *Phys. Rev. A* **81**, 062346 (2010).
- [66] S. Mostame et al., *New J. Phys.* **14**, 105013 (2012).
- [67] S. Mostame et al., *Quantum Information Processing* **16**, 44 (2017).
- [68] A. Potočník et al., *Nat. Comm.* **9**, 904 (2018).
- [69] B.-X. Wang et al., *arXiv preprint arXiv:1801.09475* (2018).
- [70] J. R. McClean, S. Boixo, V. N. Smelyanskiy, R. Babbush, and H. Neven, *arXiv preprint arXiv:1803.11173* (2018).
- [71] I. S. Ufimtsev and T. J. Martinez, *J. Chem. Theory Comput.* **5**, 2619 (2009).
- [72] N. Luehr, I. S. Ufimtsev, and T. J. Martínez, *J. Chem. Theory Comput.* **7**, 949 (2011).
- [73] C. M. Isborn, A. W. Gotz, M. A. Clark, R. C. Walker, and T. J. Martínez, *J. Chem. Theory Comput.* **8**, 5092 (2012).
- [74] Y. Tawada, T. Tsuneda, S. Yanagisawa, T. Yanai, and K. Hirao, *J. Chem. Phys.* **120**, 8425 (2004).
- [75] O. A. Vydrov and G. E. Scuseria, *J. Chem. Phys.* **125**, 234109 (2006).
- [76] K. M. Nakanishi, K. Mitarai, and K. Fujii, *arXiv preprint arXiv:1810.09434* (2018).
- [77] J. Zhang, J. Vala, S. Sastry, and K. B. Whaley, *Physical review letters* **91**, 027903 (2003).
- [78] V. V. Shende, I. L. Markov, and S. S. Bullock, *Physical Review A* **69**, 062321 (2004).
- [79] F. Vatan and C. Williams, *Phys. Rev. A* **69**, 032315 (2004).
- [80] H.-R. Wei and Y.-M. Di, *arXiv preprint arXiv:1203.0722* (2012).

SUPPLEMENTAL MATERIAL

HAMILTONIAN MANIPULATION

Consider an *ab initio* exciton model of N chromophoric monomers labelled by index A , each with two monomer electronic states labeled $|0_A\rangle$ (ground) and $|1_A\rangle$ (excited). The *ab initio* exciton Hamiltonian is

$$\hat{H} = \hat{H}^{(1)} + \hat{H}^{(2)} \quad (9)$$

$$\begin{aligned} &= \sum_A \sum_{p,q \in 0,1} (p_A|\hat{h}|q_A)|p_A\rangle\langle q_A| \\ &+ \sum_{A>B} \sum_{p,q,r,s \in 0,1} (p_A q_A|\hat{v}|r_B s_B)|p_A\rangle\langle q_A| \otimes |r_B\rangle\langle s_B| \end{aligned}$$

The real one-body matrix elements $(p_A|\hat{h}|q_A)$ are usually the (diagonal) adiabatic energy levels of the ground and first excited state of the isolated monomers, while the real two-body matrix elements $(p_A q_A|\hat{v}|r_B s_B)$ are the electrostatic interactions between the one-body densities (e.g., for $p = q$) or one-body transition densities (e.g., for $p \neq q$) of monomers A and B . These matrix elements can be computed accurately with polynomial cost (albeit expensive in absolute/prefactor considerations and requiring extensive efforts to accelerate) by *ab initio* electronic structure computations performed on classical computers, for monomers with at least several hundred atoms.

Pauli Operator Notation: The one-body operator is,

$$\begin{aligned} \hat{H}^{(1)} &= \sum_A (0_A|\hat{h}|0_A)|0_A\rangle\langle 0_A| + (1_A|\hat{h}|1_A)|1_A\rangle\langle 1_A| \quad (10) \\ &+ (0_A|\hat{h}|1_A)|0_A\rangle\langle 1_A| + (1_A|\hat{h}|0_A)|1_A\rangle\langle 0_A| \\ &= \sum_A \frac{(0_A|\hat{h}|0_A) + (1_A|\hat{h}|1_A)}{2} \hat{I}_A \\ &+ \frac{(0_A|\hat{h}|0_A) - (1_A|\hat{h}|1_A)}{2} \hat{Z}_A \\ &+ (0_A|\hat{h}|1_A) \hat{X}_A \\ &\equiv \sum_A S_A \hat{I}_A + D_A \hat{Z}_A + X_A \hat{X}_A \end{aligned}$$

Here $S_A = [(0_A|\hat{h}|0_A) + (1_A|\hat{h}|1_A)]/2$, $D_A \equiv [(0_A|\hat{h}|0_A) - (1_A|\hat{h}|1_A)]/2$, and $X_A = (0_A|\hat{h}|1_A)$. When switching to Pauli matrix notation on the second line, we use the implicit convention that any matrices not shown are taken

to be the identity, e.g., $\hat{Z}_C \equiv \hat{I}_A \otimes \hat{I}_B \otimes \hat{Z}_C \otimes I_D \otimes \dots \otimes \hat{I}_N$. Note that the off-diagonal intramonomer couplings $X_A = (0_A|\hat{h}|1_A)$ are usually defined to be zero in our exciton model convention, but there is no overhead for including them here (there will be another \hat{X}_A gate contribution below).

The two-body operator $\hat{H}^{(2)}$ requires a bit more work to convert to a form containing only sums of tensor products of Pauli operators. For each two-body term,

$$H_{AB} = \quad (11)$$

$$\begin{aligned} &(H_A|H_B)\hat{H}_A \otimes \hat{H}_B + (H_A|T_B)\hat{H}_A \otimes \hat{X}_B \\ &+ (T_A|H_B)\hat{X}_A \otimes \hat{H}_B + (T_A|T_B)\hat{X}_A \otimes \hat{X}_B \\ &+ (H_A|P_B)\hat{H}_A \otimes \hat{P}_B + (P_A|H_B)\hat{P}_A \otimes \hat{H}_B \\ &+ (T_A|P_B)\hat{X}_A \otimes \hat{P}_B + (P_A|T_B)\hat{P}_A \otimes \hat{X}_B \\ &+ (P_A|P_B)\hat{P}_A \otimes \hat{P}_B \end{aligned}$$

Here H , P , and T represent “hole,” “particle,” and “transition,” respectively. $\hat{H} \equiv [\hat{I} + \hat{Z}]/2$ and $\hat{P} \equiv [\hat{I} - \hat{Z}]/2$ are the hole and particle counting operators, respectively. Note that $\hat{I} = \hat{H} + \hat{P}$ and $\hat{Z} = \hat{H} - \hat{P}$. The two-body matrix elements are,

$$(H_A|H_B) = (0_A 0_A|\hat{v}|0_B 0_B) \quad (12)$$

$$(H_A|T_B) = (0_A 0_A|\hat{v}|0_B 1_B) = (0_A 0_A|\hat{v}|1_B 0_B) \quad (13)$$

$$(H_A|P_B) = (0_A 0_A|\hat{v}|1_B 1_B) \quad (14)$$

and so forth.

Terms 2, 3, 7, and 8 above can be written as,

$$+ (H_A|T_B)\hat{H}_A \otimes \hat{X}_B + (T_A|H_B)\hat{X}_A \otimes \hat{H}_B \quad (15)$$

$$\begin{aligned} &+ (T_A|P_B)\hat{X}_A \otimes \hat{P}_B + (P_A|T_B)\hat{P}_A \otimes \hat{X}_B \\ &= (S_A|T_B)\hat{I}_A \otimes X_B + (D_A|T_B)\hat{Z}_A \otimes X_B \\ &= + (T_A|S_B)\hat{X}_A \otimes I_B + (T_A|D_B)\hat{X}_A \otimes Z_B \end{aligned}$$

Terms 1, 5, 6, and 9 above can be written as,

$$(H_A|H_B)\hat{H}_A \otimes \hat{H}_B + (H_A|P_B)\hat{H}_A \otimes \hat{P}_B \quad (16)$$

$$+ (P_A|H_B)\hat{P}_A \otimes \hat{H}_B + (P_A|P_B)\hat{P}_A \otimes \hat{P}_B$$

$$= (S_A|S_B)\hat{I}_A \otimes \hat{I}_B + (S_A|D_B)\hat{I}_A \otimes \hat{Z}_B \quad \mathcal{X}\mathcal{X}_{AB} = (T_A|T_B) \quad (24)$$

$$+ (D_A|S_B)\hat{Z}_A \otimes \hat{I}_B + (D_A|D_A)\hat{Z}_A \otimes \hat{Z}_B \quad \mathcal{X}\mathcal{Z}_{AB} = (T_A|D_B) \quad (25)$$

In the above,

$$(S_A|T_B) = (H_A + P_A|T_B)/2 \quad (17) \quad \mathcal{Z}\mathcal{X}_{AB} = (D_A|T_B) \quad (26)$$

$$= [(H_A|T_B) + (P_A|T_B)]/2 \quad \mathcal{Z}\mathcal{Z}_{AB} = (D_A|D_B) \quad (27)$$

$$(D_A|T_B) = (H_A - P_A|T_B)/2 \quad (18) \quad \text{More specifically,}$$

$$= (H_A|T_B) - [(P_A|T_B)]/2 \quad S_A = [(0_A|\hat{h}|0_A) + (1_A|\hat{h}|1_A)]/2 \quad (28)$$

and so forth.

So the two-body Hamiltonian element can be written as,

$$D_A = [(0_A|\hat{h}|0_A) - (1_A|\hat{h}|1_A)]/2 \quad (29)$$

$$\hat{H}_{AB}^{(2)} = (S_A|S_B)\hat{I}_A \otimes \hat{I}_B \quad (19) \quad X_A = (0_A|\hat{h}|1_A) \quad (30)$$

$$+ (S_A|D_B)\hat{I}_A \otimes \hat{Z}_B + (D_A|S_A)\hat{Z}_A \otimes \hat{I}_B \quad (T_A|T_B) = (0_A 1_A|\hat{v}|0_B 1_B) \quad (31)$$

$$+ (S_A|T_B)\hat{I}_A \otimes \hat{X}_B + (T_A|S_A)\hat{X}_A \otimes \hat{I}_B \quad (T_A|S_B) = (0_A 1_A|\hat{v}|0_B 0_B + 1_B 1_B)/2 \quad (32)$$

$$+ (T_A|T_B)\hat{X}_A \otimes \hat{X}_B + (T_A|D_B)\hat{X}_A \otimes \hat{Z}_B \quad (T_A|D_B) = (0_A 1_A|\hat{v}|0_B 0_B - 1_B 1_B)/2 \quad (33)$$

$$+ (D_A|T_B)\hat{Z}_A \otimes \hat{X}_B + (D_A|D_B)\hat{Z}_A \otimes \hat{Z}_B \quad (S_A|T_B) = (0_A 0_A + 1_A 1_A|\hat{v}|0_B 1_B)/2 \quad (34)$$

Hamiltonian in Pauli Notation: After the straightforward algebra above, the total Hamiltonian can be written as,

$$\hat{H} = \mathcal{E} + \mathcal{H}^{(1)} + \mathcal{H}^{(2)} = \mathcal{E}\hat{I} + \sum_A \mathcal{Z}_A \hat{Z}_A + \mathcal{X}_A \hat{X}_A \quad (20) \quad (D_A|T_B) = (0_A 0_A - 1_A 1_A|\hat{v}|0_B 1_B)/2 \quad (35)$$

$$+ \sum_{A>B} \mathcal{X}\mathcal{X}_{AB} \hat{X}_A \otimes \hat{X}_B + \mathcal{X}\mathcal{Z}_{AB} \hat{X}_A \otimes \hat{Z}_B \quad (S_A|S_B) = (0_A 0_A + 1_A 1_A|\hat{v}|0_B 0_B + 1_B 1_B)/4 \quad (36)$$

$$+ \mathcal{Z}\mathcal{X}_{AB} \hat{Z}_A \otimes \hat{X}_B + \mathcal{Z}\mathcal{Z}_{AB} \hat{Z}_A \otimes \hat{Z}_B \quad (S_A|D_B) = (0_A 0_A + 1_A 1_A|\hat{v}|0_B 0_B - 1_B 1_B)/4 \quad (37)$$

The matrix elements are,

$$\mathcal{E} = \sum_A S_A + \sum_{A>B} (S_A|S_B) \quad (21) \quad (D_A|S_B) = (0_A 0_A - 1_A 1_A|\hat{v}|0_A 0_B + 1_A 1_B)/4 \quad (38)$$

$$\mathcal{Z}_A = D_A + \sum_B (D_A|S_B) \quad (22) \quad (D_A|D_B) = (0_A 0_A - 1_A 1_A|\hat{v}|0_A 0_B - 1_A 1_B)/4 \quad (39)$$

$$\mathcal{X}_A = X_A + \sum_B (T_A|S_B) \quad (23)$$

Note that $\{\mathcal{Z}_A\}$ are expected to be the largest matrix elements in this Hamiltonian, and are of the order of a few eV (10^{-2} – 10^{-1} au). In practice, we typically find the $\{\mathcal{X}_A\}$ and $\{\mathcal{X}\mathcal{X}_{AB}\}$ are the next largest matrix elements (10^{-3} – 10^{-2} au). These are rough estimates which may differ in specific systems.

$$\theta_{MN} = \cos^{-1}(\mu/(\sin(\theta_0)\sin(\theta_{AB})\sin(\theta_{BC})\dots\sin(\theta_{LM}))) \quad (55)$$

Note that the last angle θ_{MN} is only resolved up to a phase factor of ± 1 : the explicit value of η must be checked using the last line of the forward formula above to determine the phase factor (the relative error will be 0 [+1] or 2 [-1], which makes the check particularly easy).

The “interference” state $(|\Phi_\Theta\rangle \pm |\Phi_{\Theta'}\rangle)/\sqrt{2}$ can easily be formed by substitutions of the coefficients

$$\mu^\pm = (\mu^\Theta \pm \mu^{\Theta'})/\sqrt{2} \quad (56)$$

$$\alpha^\pm = (\alpha^\Theta \pm \alpha^{\Theta'})/\sqrt{2} \quad (57)$$

$$\vdots \quad (58)$$

Note that the CIS state with $\mu = 0, \alpha = \beta = \gamma = \dots = 1/\sqrt{N}$ is usually called the $|W_N\rangle$ state. A circuit for the $|W_N\rangle$ that was used as the basis for this work is presented in [57].

VQE Global Entangler Matrix: In any configuration-space basis, the adiabatic eigenfunctions of the real electronic or *ab initio* exciton Hamiltonian can be written as real, orthonormal vectors with arbitrary total phase of ± 1 . Therefore, the VQE entangler operator \hat{U} can be restricted to $SO(2^N)$ without loss. We have elected to construct the total VQE entangler circuit for the *ab initio* exciton model by placing a two-body entangler restricted to $SO(4)$ at each two-body interaction site in the exciton Hamiltonian. E.g., for a linear arrangement,



If additional variational flexibility in the ansatz is desired, a straightforward approach is to add additional layers of entanglers of the form shown here, or to extend two-body entanglers to the next layer(s) of nearest neighbors.

Details of the specific VQE two-body entangler \hat{U}_2 restricted to $SO(4)$ that is used in this work are presented below - these manipulations are intended to produce a VQE two-body entangler whose parameters are easy to guess (e.g., starting from all zeros) and to optimize with partial gradient information (e.g., by simple gradient-descent or L-BFGS) for problems encountered in the *ab initio* exciton model.

Note that there has been much interest in the literature on the construction of optimal 2-body quantum circuits covering $SU(4)$ or $SO(4)$ using various or arbitrary gate libraries - for an overview, see [77–80].

VQE Two-Body Entangler Matrix: $SO(4)$ is the group of real, orthogonal matrices with determinant +1, and covers all possible two-body entangler matrices needed in our VQE task. There are infinitely many equivalent logical parametrizations of $SO(4)$ with 6 real parameters, but some of these will prove easier to optimize than others in VQE applications.

For instance, one particularly straightforward

parametrization of $SO(4)$ is given by,

$$\hat{U}_2 = \exp \left(\begin{bmatrix} 0 & +A & +B & +C \\ -A & 0 & +D & +E \\ -B & -D & 0 & +F \\ -C & -E & -F & 0 \end{bmatrix} \right) \quad (60)$$

That is, any special orthogonal matrix for $N = 4$ can be written as the matrix exponential of an $N = 4$ antisymmetric matrix with 6 unconstrained real parameters A through F .

Another, equivalent parametrization can be realized by considering the two-body Pauli generators of the antisymmetric group,

$$-i\hat{Y}_A \otimes \hat{I}_B = \begin{bmatrix} 0 & 0 & -1 & 0 \\ 0 & 0 & 0 & -1 \\ +1 & 0 & 0 & 0 \\ 0 & +1 & 0 & 0 \end{bmatrix} \quad (61)$$

$$-i\hat{Y}_A \otimes \hat{X}_B = \begin{bmatrix} 0 & 0 & 0 & -1 \\ 0 & 0 & -1 & 0 \\ 0 & +1 & 0 & 0 \\ +1 & 0 & 0 & 0 \end{bmatrix} \quad (62)$$

$$-i\hat{Y}_A \otimes \hat{Z}_B = \begin{bmatrix} 0 & 0 & -1 & 0 \\ 0 & 0 & 0 & +1 \\ +1 & 0 & 0 & 0 \\ 0 & -1 & 0 & 0 \end{bmatrix} \quad (63)$$

$$-i\hat{I}_A \otimes \hat{Y}_B = \begin{bmatrix} 0 & -1 & 0 & 0 \\ +1 & 0 & 0 & 0 \\ 0 & 0 & 0 & -1 \\ 0 & 0 & +1 & 0 \end{bmatrix} \quad (64)$$

$$-i\hat{X}_A \otimes \hat{Y}_B = \begin{bmatrix} 0 & 0 & 0 & -1 \\ 0 & 0 & +1 & 0 \\ 0 & -1 & 0 & 0 \\ +1 & 0 & 0 & 0 \end{bmatrix} \quad (65)$$

$$-i\hat{Z}_A \otimes \hat{Y}_B = \begin{bmatrix} 0 & -1 & 0 & 0 \\ +1 & 0 & 0 & 0 \\ 0 & 0 & 0 & +1 \\ 0 & 0 & -1 & 0 \end{bmatrix} \quad (66)$$

Therefore,

$$\hat{U}_2 = \exp(\quad (67)$$

$$\begin{aligned} & -i\theta_{XY}\hat{X}_A \otimes \hat{Y}_B - i\theta_{ZY}\hat{Z}_A \otimes \hat{Y}_B - i\theta_{YZ}\hat{Y}_A \otimes \hat{Z}_B \\ & -i\theta_{YX}\hat{Y}_A \otimes \hat{X}_B - i\theta_{YI}\hat{Y}_A \otimes \hat{I}_B - i\theta_{IY}\hat{I}_A \otimes \hat{Y}_B \end{aligned}$$

with the six real parameters θ_{IY} , θ_{YI} , θ_{XY} , θ_{YX} , θ_{ZY} , and θ_{YZ} . The correspondence between parameter sets is,

$$A = -(\theta_{IY} + \theta_{ZY}) \quad (68)$$

$$F = -(\theta_{IY} - \theta_{ZY}) \quad (69)$$

$$C = -(\theta_{YX} + \theta_{XY}) \quad (70)$$

$$D = -(\theta_{YX} - \theta_{XY}) \quad (71)$$

$$B = -(\theta_{YI} + \theta_{YZ}) \quad (72)$$

$$E = -(\theta_{YI} - \theta_{YZ}) \quad (73)$$

We have found that the second parametrization of the VQE two-body entangler is sometimes easier to optimize than the first, e.g., when using straightforward gradient descent with finite-difference gradients, and using an initial guess of zero entanglement (all angles $\{\theta_{IY} \dots \theta_{YZ}\}$ or antisymmetric generator parameters $\{A \dots F\}$ set to zero). With tightly converged optimizations using L-BFGS, both logical parametrizations of the two-body entanglers produce results with similar accuracy in *ab initio* exciton model excitation energies and oscillators strengths.

We note that there are many possible physical realizations of two-body entangler gates covering $SO(4)$, depending on the specific gate library of a given quantum

computer. For instance, one possible two-body entangler circuit is [80],

$$\begin{aligned} |0_A\rangle & \text{---} [R_y(\theta_1)] \text{---} \bullet \text{---} [R_y(\theta_3)] \text{---} \bullet \text{---} [R_y(\theta_5)] \text{---} \\ |0_B\rangle & \text{---} [R_y(\theta_2)] \text{---} \oplus \text{---} [R_y(\theta_4)] \text{---} \oplus \text{---} [R_y(\theta_6)] \text{---} \end{aligned} \quad (74)$$

In practice, it seems important to consider different possible logical parametrizations of the two-body entangler circuits, regardless of the underlying physical parametrization. To highlight this, we note that direct optimization of the two-body entanglers in terms of the angles $\{\theta_1 \dots \theta_6\}$ in Equation 74 did not converge to the same qualitative solution as Equations 60 or 67 above, when using steepest descent (though this circuit converged to a local minimum without apparent convergence difficulties). In fact, the solution obtained with the parametrization of Equation 74 was not qualitatively superior to the CIS polynomial-scaling classical solution. Since the circuit in Equation 74 covers $SO(4)$ just as well as the logical parametrizations of Equations 60 or 67, it likely the case that the all-zeros guess lies in the neighborhood of an undesired local minimum. Switching to L-BFGS, the two-body entanglers of Equation 74 eventually converge to the same qualitative solution as in Equations 60 or 67, but some convergence difficulties are encountered, and a the L-BFGS optimization takes approximately twice as many iterations. The selection of an optimal logical parametrization of the entangler circuits, mapping to physical parametrization in terms of available gate library, and design of algorithms for robust convergence to the desired MC-VQE minimum is obviously a subject worth further consideration in future work.

All results depicted in the primary manuscript use a logical two-body entangler circuit parametrized by Equation 67, and optimized by L-BFGS with finite-difference gradients (second-order symmetric with $\Delta\theta = 0.01$), and using an initial guess of zero entanglement with all angles $\{\theta_{IY} \dots \theta_{YZ}\}$ starting at zero.

Example output files of the optimization profiles with steepest descent and L-BFGS and using the various parametrizations of the two-body entanglers shown above are provided for an $N = 12$ subset of the B850 ring complex in the supplementary data packet.

COMPUTATIONAL DETAILS

All computational results for the B850 ring were run with QUASAR GIT SHA 4ce64a05a0f5f63988cb68209d24e085d2de275f.

The XYZ geometry of the $N = 18$ BChl-*a* LH2 B850 ring complex is contained in the supplemental data packet. Monomer energies, densities, and dipole/transition-dipole moments (relative to center of

mass) are computed for each monomer in isolation using ω PBE($\omega = 0.3$)/6-31G*. Ground-state DFT is used to compute the ground state, Tamm-Dancoff Approximation TD-DFT (TDA-TD-DFT) is used to compute the excited state. The S_1 total and $S_0 - S_1$ transition dipole moment are computed without orbital response (unrelaxed). Two-body interaction matrix elements are computed between monomers using the dipole-dipole interaction formula,

$$V_{AB} = \frac{\vec{\mu}_A \cdot \vec{\mu}_B - 3(\vec{\mu}_A \cdot \vec{n}_{AB})(\vec{\mu}_B \cdot \vec{n}_{AB})}{r_{AB}^3} \quad (75)$$

Here $\vec{\mu}_A$ is the total or transition dipole moment, \vec{n}_{AB} is the normal vector along the displacement between the centers of mass of monomers A and B , and r_{AB} is the distance between the centers of mass of monomers A and B .

The dipole oscillator strength is computed from the energy gaps and transition dipole moments between approximate eigenstates,

$$O_{\Theta\Theta'} = \frac{2}{3}(E_{\Theta'} - E_{\Theta})\langle\Psi_{\Theta}|\hat{\mu}|\Psi_{\Theta'}\rangle^2 \quad (76)$$

The dipole operators can be written as sums of 1-body Pauli operators, e.g.,

$$\hat{\mu} \equiv \sum_A \vec{\mu}_I^A \hat{I}_A + \vec{\mu}_Z^A \hat{Z}_A + \vec{\mu}_X^A \hat{X}_A \quad (77)$$

where $\vec{\mu}_I^A = (\vec{\mu}_A^{11} + \vec{\mu}_A^{00})/2$, $\vec{\mu}_Z^A = (\vec{\mu}_A^{11} - \vec{\mu}_A^{00})/2$, and $\vec{\mu}_X^A = \vec{\mu}_A^{01}$ are computed from the monomer total and transition dipole moments.

To aid in replication of the results the total energies of the S_0 and S_1 states of each monomer are provided in Table I. The classical monomer quantum chemistry outputs from TERAChem and full numerical details of the *ab initio* exciton Hamiltonian for this system are present in the supplemental data packet. For the full $N = 18$ BChl-*a* B850 ring complex system in LH2, the L-BFGS iterative history, optimized MC-VQE parameter values, and other characteristics of the converged MC-VQE solution are present in the QUASAR output file and .NPZ data file in the supplemental data packet.

ADDITIONAL CASE STUDY: BCHL-A H-AGGREGATE STACK

At the request of a reviewer, we have additionally considered a test case where CIS performs markedly poorly, to verify that MC-VQE continues to provide accurate results for systems with qualitatively more multi-excitonic character than the simple J -aggregate-type B850 ring complex studied in the main manuscript. To that end, we have considered a linear stack of $N = 8$ truncated BChl-*a* units, stacked in an aligned geometry and then allowed

TABLE I: Monomer S_0 and S_1 state energies for $N = 18$ BChl-*a* LH2 B850 ring complex computed at ω PBE($\omega = 0.3$)/6-31G* using DFT and TDA-TD-DFT.

A	E_{S_0}	E_{S_1}
1	-2263.26377175	-2263.19429617
2	-2263.25985281	-2263.18713945
3	-2263.26107440	-2263.18942087
4	-2263.27390235	-2263.20150610
5	-2263.24311586	-2263.17416282
6	-2263.29019565	-2263.21759301
7	-2263.25812333	-2263.18493523
8	-2263.31462943	-2263.24431121
9	-2263.28358218	-2263.21345739
10	-2263.23436184	-2263.16413403
11	-2263.27574682	-2263.20553908
12	-2263.28354903	-2263.21341881
13	-2263.28916608	-2263.21882588
14	-2263.27286521	-2263.20307447
15	-2263.27213702	-2263.20127737
16	-2263.29074598	-2263.22183660
17	-2263.27479708	-2263.20232022
18	-2263.29686920	-2263.22028791

to geometrically relax with ω PBE($\omega = 0.3$)/6-31G*-D3. An *ab initio* exciton model was constructed for this system using the same TDA-TD-DFT ω PBE($\omega = 0.3$)/6-31G* treatment of the monomers and unrelaxed dipole-dipole couplings as described elsewhere for the B850 ring complex. The lowest 9 states and 8 ground-to-excited oscillator strengths were computed with FCI, CIS, and MC-VQE. For the MC-VQE computations, a slightly updated version of our QUASAR code was used, with the same overall topology of two-layer linear VQE entangler circuit depicted in Equation 59 and with the two-body entanglers constructed as in 74, and with redundant \hat{R}_y gates at the interface between the two layers of two-body entanglers removed. The gradient-free Powell method was used to tightly optimize the state-averaged VQE entangler circuit parameters to a maximum state-averaged energy gradient of 1×10^{-7} . The specific geometry, .NPZ file containing *ab initio* exciton model matrix elements, QUASAR output file (including state-averaged VQE entangler circuit construction and optimized parameters), and .NPZ file containing the output state energies and oscillator strengths are provided in the supplemental data packet.

The stacking geometry of the chromophores in this case study promotes H -aggregate-type electronic behavior, wherein the monomer states split and generally blue shift, and the oscillator strengths of the lowest few states are heavily attenuated relative to higher-lying states. Double and higher-lying excitations strongly modulate the energies, characters, and oscillator strengths of the adiabatic electronic states for this system. As such, CIS performs extremely poorly relative to FCI for this system, as depicted in Figure 3: the CIS excitation en-

ergies are all blue-shifted by between 0.1 and 0.5 eV from the FCI excitation energies, and the CIS oscillator strengths are often qualitatively incorrect (e.g., relative errors in the vicinity of 100% for states with significant oscillator strengths). Even the apparent agreement of CIS and FCI oscillator strengths for the brightest transition between S_0 and S_7 is accidental: examination of the S_7 excited state populations of the monomers $P_A^\Theta \equiv \langle \Psi_\Theta | 1_A \rangle \langle 1_A | \Psi_\Theta \rangle$ indicates that the majority of the exciton lives on monomers 3 and 4 in zero-based ordering (with more-minor contributions on monomers 0 and 1) in FCI, but the corresponding CIS state has the majority of the exciton on monomer 2 and then spread to monomers 3, 4, and 5, i.e., the state characters are markedly different. In more numerical terms, the fidelity between FCI and CIS is $|\langle \Psi_7^{\text{FCI}} | \Psi_7^{\text{CIS}} \rangle| = 0.688$, while the corresponding fidelity between FCI and MC-VQE is $|\langle \Psi_7^{\text{FCI}} | \Psi_7^{\text{VQE}} \rangle| = 0.995$. Therefore, the agreement of oscillator strengths between CIS and FCI for this state is purely accidental, and CIS produces an absorption spectrum profile which is both qualitatively and quantitatively incorrect. By contrast, MC-VQE (starting from the *same* CIS contracted reference states) produces an absorption spectrum profile which is generally visually indistinguishable from FCI, and which agrees in the details of the state characters, without requiring modifications to the topology of the state-averaged VQE entangler circuit. The MC-VQE excitation energies are generally in error with FCI by at most 0.01 eV, while the corresponding oscillator strengths are generally in error with FCI by at most 0.1 [-]. Inspection of the excited state populations indicates that the state characters are highly congruent between FCI and MC-VQE. The agreement of MC-VQE and FCI is not quite as perfect as the $N = 18$ B850 ring in the main text, but the improvement of MC-VQE over CIS is much more striking. Overall, this case study provides compelling evidence that MC-VQE can provide reliable results for difficult problems involving significant multi-excitonic character, all while starting from poor-quality CIS contracted reference states and without modifying the nature of the state-averaged VQE entangler circuit.

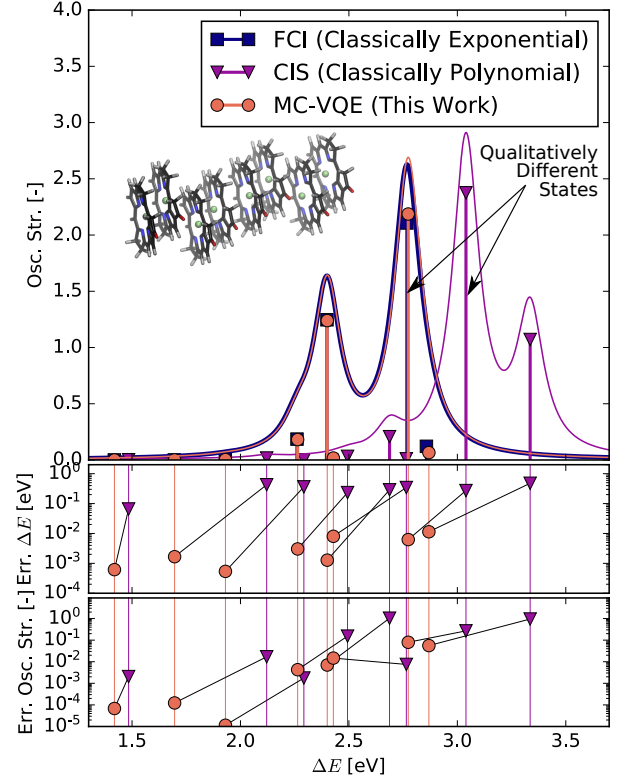


FIG. 3: (color online). Top - Simulated absorption spectrum of $N = 8$ linear stack BChl-a test case (geometry depicted in inset), computed from the excitation energies and oscillator strengths of the lowest 8 electronic transitions, depicted as vertical sticks. The envelope of the absorption spectrum is sketched by broadening the contribution from each transition with a Lorentzian with width of $\delta = 0.15$ eV. The simulated MC-VQE and reference FCI results are largely visually indistinguishable. Middle - errors in excitation energies. Bottom - errors in oscillator strengths. Middle and bottom - thin lines are a guide for the eye.